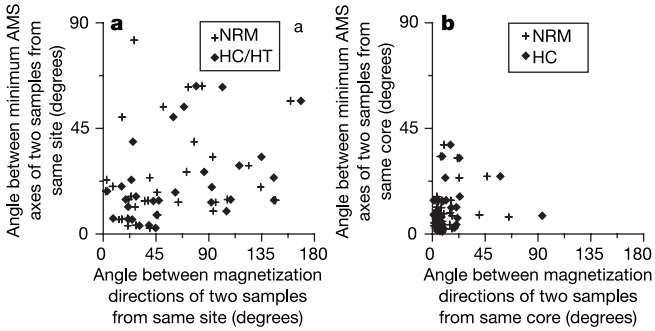

Figure 4 Comparison of the angular distance between minimum anisotropy of magnetic susceptibility (AMS) axes and magnetization component directions between two samples. **a**, Two samples from the same site; **b**, two samples from the same core. NRM, natural remanent magnetization direction; HC/HT, high coercivity or high temperature remanent magnetization direction; both are shown for comparison.

the Earth's) at a distance of 100 km that lasts for 100 s after an impact[18]. For Vredefort, these are minimum values because the meteorite diameter was greater than 10 km (ref. 19).

We suggest that small-wavelength magnetic fields of high intensity are responsible for both the randomization and the unusually high remanence of the Vredefort basement rocks. Diamond anvil experiments on magnetite show that its remanent saturation moment is significantly enhanced when it is either under pressure or after decompression[20]. This implies that shock creates a piezo-remanent magnetization, or a high-field TRM, depending on how fast the newly formed magnetite grains cooled through the Curie temperature, which is 580 °C at 0.1 MPa yet 1,180 °C at 30 GPa (refs 21, 22). Both processes would increase, not decrease, the magnetic intensities of the shocked rocks. Assuming that the temperature of the pre-impact crust was 500 °C, magnetite grains crystallizing in a 1-μm-thick PDF plane would cool through the Curie point in less than one second[7,23], in the plasma generated field. In contrast, a 1-m-wide dyke takes about 11 days to cool[23], long after the plasma field disappeared, in the presence of a 'normal' Earth field.

Aeromagnetic surveys over meteorite impacts commonly detect field intensities lower than regional magnetic trends[24]. Such is also the case for the gigantic (>1,000 km diameter) martian impact basins Hellas and Argyre[1], whose lower field intensities are commonly ascribed to pressure demagnetization[2,3]. Our study of Vredefort, the best terrestrial analogue of a martian meteorite crater, demonstrates that shock in fact leads to intensified and randomized magnetic vectors in shocked rocks. On the scale of the crater, the vectors cancel out, being equivalent to a volume of non-magnetic material seen at high altitudes, thus accounting for the reduced fields measured over the craters. The lack of crustal magnetism over impact basins on Mars is commonly ascribed to the absence of an internal dynamo during meteorite impact. Our new findings question the validity of this assumption. □

Received 18 October 2004; accepted 10 March 2005; doi:10.1038/nature03560.

1. Acuña, M. H. *et al.* Global distribution of crustal magnetization discovered by the Mars Global Surveyor MAG/ER experiment. *Science* **284,** 790–793 (1999).
2. Hood, L. L., Richmond, N. C., Pierazzo, E. & Rochette, P. Distribution of crustal magnetic fields on Mars: Shock effects of basin-forming impacts. *Geophys. Res. Lett.* **30,** 1281, doi:10.1029/2002GL016657 (2003).
3. Mohit, P. S. & Arkani-Hamed, J. Impact demagnetization of the Martian crust. *Icarus* **168,** 305–317 (2004).
4. Moser, D. E. Dating the shock wave and thermal imprint of the giant Vredefort impact, South Africa. *Geology* **25,** 7–10 (1997).
5. Stöffler, D. & Langenhorst, F. Shock metamorphism of quartz in nature and experiment: I. Basic observation and theory. *Meteoritics* **29,** 155–181 (1994).
6. Grieve, R. A. F., Langenhorst, F. & Stöffler, D. Shock metamorphism of quartz in nature and experiment: II. Significance in geoscience. *Meteoritics* **31,** 6–35 (1996).
7. Cloete, M. *et al.* Characterization of magnetite particles in shocked quartz by means of electron- and magnetic force microscopy: Vredefort, South Africa. *Contrib. Mineral. Petrol.* **137,** 232–245 (1999).
8. Hart, R. J., Hargraves, R. B., Andreoli, M. A. G., Tredoux, M. & Doucouré, C. M. Magnetic anomaly near the center of the Vredefort structure: implications for impact-related magnetic signatures. *Geology* **23,** 277–280 (1995).
9. Hart, R. J. *et al.* 'Super magnetic' rocks generated by shock metamorphism from the center of the Vredefort impact structure, South Africa. *S. Afr. J. Geol.* **103,** 151–155 (2000).
10. Hargraves, R. B. Paleomagnetic evidence relevant to the origin of the Vredefort ring. *J. Geol.* **78,** 253–263 (1970).
11. Jackson, G. M. *Paleomagnetic Study and Magnetic Modeling of the Vredefort Dome*. Thesis, Univ. Witwatersrand (1982).
12. Hargraves, R. B. & Roy, D. W. Paleomagnetism of anorthosite in and around the Charlevoix cryptoexplosion structure, Quebec. *Can. J. Earth Sci.* **11,** 854–859 (1974).
13. Halls, H. C. Shock-induced remanent magnetization in late Precambrian rocks from Lake Superior. *Nature* **255,** 692–695 (1975).
14. Clark, D. A. & Emerson, D. W. Notes on rock magnetic characteristics in applied geophysical studies. *Exp. Geophys.* **22,** 547–555 (1991).
15. Gilder, S. & McNulty, B. Tectonic exhumation and tilting of the Mount Givens pluton, central Sierra Nevada, California. *Geology* **27,** 919–922 (1999).
16. Wennerström, M. & Airo, M. L. Magnetic fabric and emplacement of the post-collisional Pomovaara Granite Complex in northern Fennoscandia. *Lithos* **45,** 131–145 (1998).
17. Crawford, D. A. & Schultz, P. H. Laboratory observations of impact-generated magnetic fields. *Nature* **336,** 50–52 (1988).
18. Crawford, D. A. & Schultz, P. H. Electromagnetic properties of impact-generated plasma, vapor and debris. *Int. J. Impact Eng.* **23,** 169–180 (1999).
19. Turtle, E. P. & Pierazzo, E. Constraints on the size of the Vredefort impact crater from numerical modeling. *Meteorit. Planet. Sci.* **33,** 483–490 (1998).
20. Gilder, S. A., LeGoff, M., Chervin, J. C. & Peyronneau, J. Magnetic properties of single and multi-domain magnetite under pressures from 0 to 6 GPa. *Geophys. Res. Lett.* **31,** L10612, doi:10.1029/2004GL019844 (2004).
21. Samara, G. & Giardini, A. Effect of pressure on the Néel temperature of magnetite. *Phys. Rev.* **186,** 577–580 (1969).
22. Schult, A. Effect of pressure on the Curie temperature of titanomagnetites [$(1-x)\cdot Fe_3O_4$–$x\cdot TiFe_2O_4$]. *Earth Planet. Sci. Lett.* **10,** 81–86 (1970).
23. Turcott, D. L. & Schubert, G. *Geodynamics* (Wiley & Sons, New York, 1982).
24. Grieve, R. A. F. & Pilkington, M. The signature of terrestrial impacts. *J. Austr. Geol. Geophys.* **16,** 399–420 (1996).
25. Nel, L. T. *Geological Map of the Country Around Vredefort. Scale 1:63360* (Union of S. Afr., Dept Mines and Ind., Geol. Surv., Pretoria, 1927).

Acknowledgements We thank A. Galdeano, G. Hulot, M. Cloete, M. Le Goff, Y. Gallet and G. Plenier for discussions and comments. This work was supported by the French Ministries of Foreign Affairs and Education and Research, INSU and the South African National Research Foundation.

Competing interests statement The authors declare that they have no competing financial interests.

Correspondence and requests for materials should be addressed to S.A.G. (gilder@ipgp.jussieu.fr).

Advanced optics in a jellyfish eye

Dan-E. Nilsson[1], Lars Gislén[2], Melissa M. Coates[1], Charlotta Skogh[1] & Anders Garm[1]

[1]*Department of Cell and Organism Biology, Lund University, Zoology Building, Helgonavägen 3, 22362 Lund, Sweden*
[2]*Department of Theoretical Physics, Lund University, Sölvegatan 14A, SE - 223 62 Lund, Sweden*

Cubozoans, or box jellyfish, differ from all other cnidarians by an active fish-like behaviour and an elaborate sensory apparatus[1,2]. Each of the four sides of the animal carries a conspicuous sensory club (the rhopalium), which has evolved into a bizarre cluster of different eyes[3]. Two of the eyes on each rhopalium have long been known to resemble eyes of higher animals, but the function and performance of these eyes have remained unknown[4]. Here we show that box-jellyfish lenses contain a finely tuned refractive index gradient producing nearly aberration-free imaging. This demonstrates that even simple animals have been able to evolve the sophisticated visual optics previously known only from a few

advanced bilaterian phyla. However, the position of the retina does not coincide with the sharp image, leading to very wide and complex receptive fields in individual photoreceptors. We argue that this may be useful in eyes serving a single visual task. The findings indicate that tailoring of complex receptive fields might have been one of the original driving forces in the evolution of animal lenses.

In the light of the current interest in early eye evolution[5,6], the uniquely evolved eyes of box jellyfish have been neglected. To a much higher degree than other jellyfish, cubozoan medusae actively position themselves in suitable habitats[1,7]. This is the likely reason that they have eyes rivalling those of advanced Bilateria. Suspended from the sides of the bell, each box jellyfish carries four sensory clubs (rhopalia), and each of these is equipped with two lens eyes, here termed the upper and lower eyes, together with two different pairs of simpler pigment-pit eyes[2,3,8–10] (Fig. 1), making a total of 24 eyes per animal. From the unique crystallin proteins we know that at least the lenses have evolved independently in box jellyfish[11,12]. Making good lenses seems to be a demanding task, because only few animal phyla have accomplished it[13]. Our question here is whether the eyes of box jellyfish are simple sensory organs or whether they have, to any degree, managed to evolve the sophisticated optics found in vertebrate and cephalopod eyes[14], giving them image-forming capabilities.

The eyes do not vary much between box jellyfish species, and for convenience we used a small (10 mm) Caribbean species, *Tripedalia cystophora*, which can be bred from polyps under laboratory conditions[15]. The natural habitat of this species is among the prop roots around the edge of mangrove lagoons[1]. To investigate the visual optics we first established accurate geometrical models of the upper and lower lens eyes (Fig. 1d). These have diameters of 150 and 250 μm respectively. Both eyes are built similarly but differ somewhat in retinal geometry. All major components of a typical camera-type eye are present: a cornea, a lens, a retina, a pigment layer and an iris. The lenses are spherical and cellular. A thin cellular space separates the lens from the retina. Microvilli projecting from the ciliary outer segments of photoreceptor cells fill the retina[3]. The outer segments are contiguous and lack structures that can act as light guides. They are arranged in an orderly way but have their long axes unconventionally aligned towards a point just outside the pupil in the lower eye and obliquely towards the pupil margin in the upper eye (Fig. 1d). A layer of dark pigment covers the outside of the retina and forms an iris around the lens. Changing the light intensity reveals that the lower eye has a mobile pupil that can close down the aperture from about 150 μm to 100 μm in less than 1 min (Fig. 1), whereas the pupil of the upper eye remains constant at all intensities.

Fresh isolated lenses are able to form good images (Fig. 2) irrespective of lens orientation, implying spherically symmetrical optics. Using microinterferometry we determined the refractive index from the periphery to the centre of the lenses. From the data (Fig. 2) it is clear that the lenses of both eyes contain refractive index gradients. The central refractive index is about 1.48, which is a little lower than the 1.49–1.56 found in fish lenses[14,16]. In the upper eye the lenses display a smooth gradual decrease in refractive index towards the periphery, whereas lenses of the lower eye have a nearly homogeneous core surrounded by a smooth gradient. In the lens periphery of both eyes the refractive index gradient falls without discontinuity to the value of the surrounding tissue (1.34). Electron microscopic sections of the cellular lenses reveal a corresponding staining gradient, indicating that the packing density of crystallin proteins is responsible for the gradient in refractive index.

Tracing rays through the refractive-index gradient of the upper eye reveal nearly perfect focusing for all ray positions (Fig. 2). For such a minute eye it is surprising to find well-corrected, aberration-free imaging, otherwise known only from the much larger eyes of vertebrates and cephalopods[13,14,16]. The gradient in the upper-eye lenses comes very close to the ideal solution[17]. The lenses of the lower eye have a less ideal gradient and consequently display some spherical aberration (Fig. 2e, f). It is the homogeneous lens core and steep peripheral gradient that results in positive spherical aberration in the lower eye.

When the ray paths of the lenses are put into the geometrical models of the eyes, it turns out that both eyes are severely under-focused (Fig. 3a). The sharp image falls well below the retina and it would seem that the sharp focus of the lenses is wasted by inappropriate eye geometry. Another, more likely, interpretation is that the eyes are 'purposely' under-focused to remove high spatial frequencies (fine image details) from the retinal image, much as occurs in insect dorsal ocelli[18]. If the arrangement is indeed a spatial

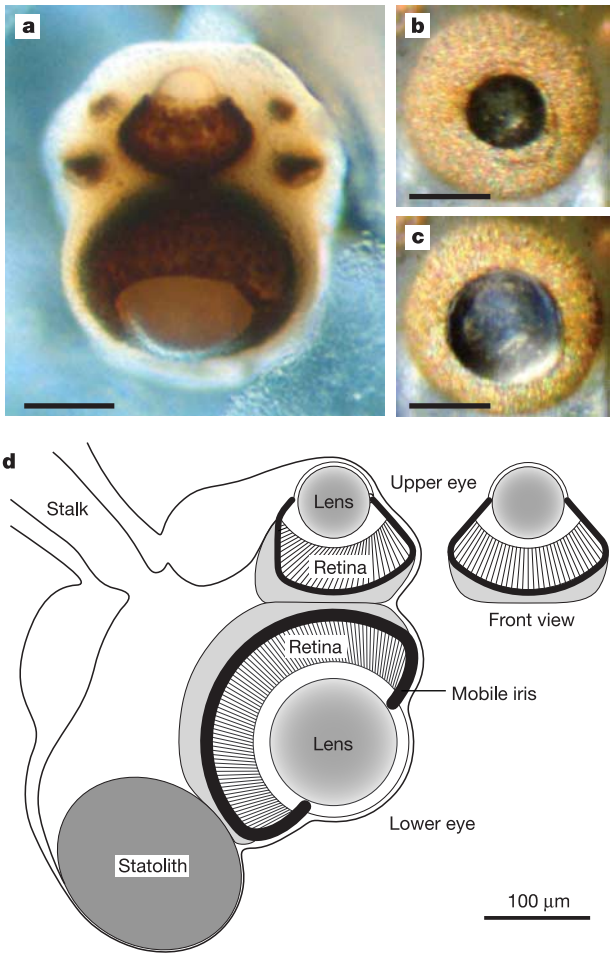

Figure 1 The eyes of the box jellyfish *Tripedalia cystophora*. **a**, The rhopalium shows the upper and lower lens eyes flanked by two pairs of simpler eyes. **b**, **c**, The live lower eye displays a mobile pupil. In **b** the eye was exposed for about 10 min to light intensities corresponding to direct sunlight, which is enough to close the pupil maximally. The fully open pupil in **c** is the result of total darkness for 10 min. Pupil adjustments take about 1 min. **d**, An accurate anatomical model. The sagittal section contains the statolith and the internal structure of the two lens eyes. The spherical lenses are surrounded by a cellular capsule, the inner part of which forms the equivalent of a vitreous body between lens and retina. Iris constriction in the large eye is caused by contraction of the outer part of the lens capsule. The lower eye is rotationally symmetrical, but the upper eye is only bilaterally symmetrical (front view shown to the right). Receptor outer segments fill the retina of both lens eyes. The alignment of receptor outer segments is unusual, especially in the upper eye, where receptor axes converge on a point at one side of the lens. Scale bars, 100 μm.

low-pass filter, it would help the animals to detect the large and stationary structures of their visual environment, but would leave unseen the plankton and small particles floating with the current. Assuming that the lens eyes have evolved to allow the jellyfish to remain in nearshore habitats and to avoid swimming into obstacles, a low-pass filtering of image structure would make sense.

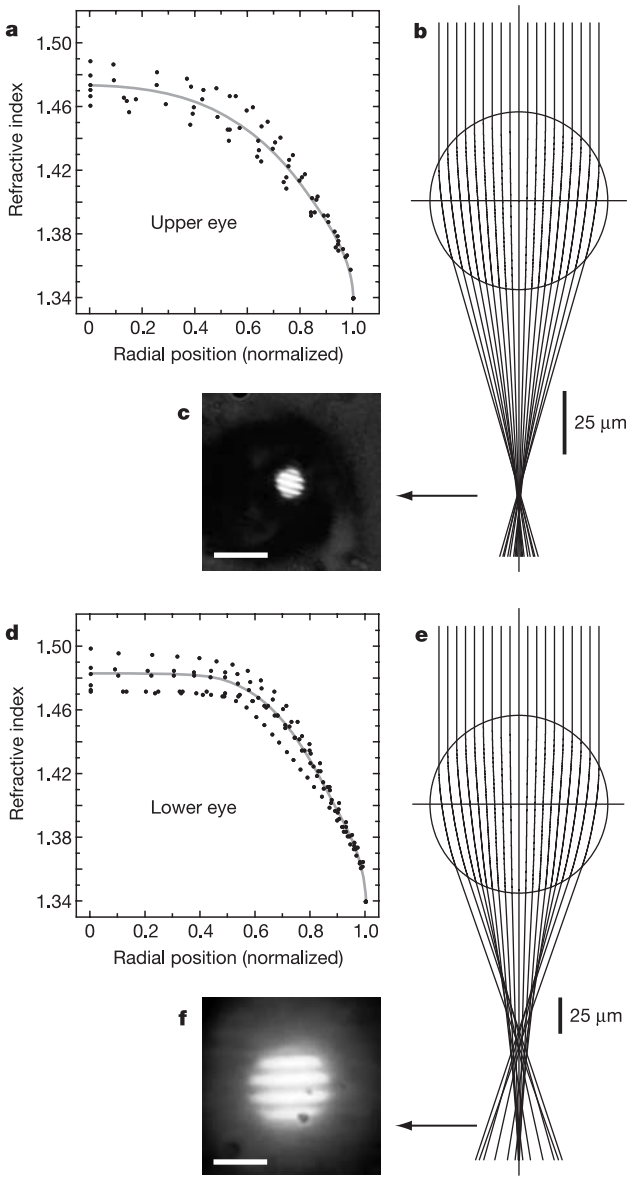

Figure 2 Optical properties of the lenses. **a**–**c**, Upper eye; **d**–**f**, lower eye. In **a** and **d** the refractive index is plotted as a function of radial position in the lenses (values from six lenses of each kind, normalized to unity radius). In the upper-eye lens (**a**) the refractive index follows a near-parabolic profile, whereas the lower-eye lens (**d**) has a homogeneous centre and a gradient only in the outer half. Curves fitted to the data (grey traces in **a** and **d**) were used to calculate the ray paths in **b** and **e**. From these it is obvious that the lens of the upper eye forms a much better image than that of the lower eye. The upper-eye lens produces an almost aberration-free focus at a distance of 3.3 radii from the lens centre, whereas the lower-eye lens displays positive spherical aberration, with focal lengths ranging from 2.6 to 3.7 lens radii. **c**, **f**, The difference in image quality was confirmed by direct observation of images produced behind fresh isolated lenses. A grating object at infinity generates a crisp image behind a lens of the upper eye (**c**), but the same object imaged by a lens from a lower eye is contaminated by considerable aberration blur (**f**). The difference in image magnification is a consequence of the different focal lengths. Scale bars, 25 μm.

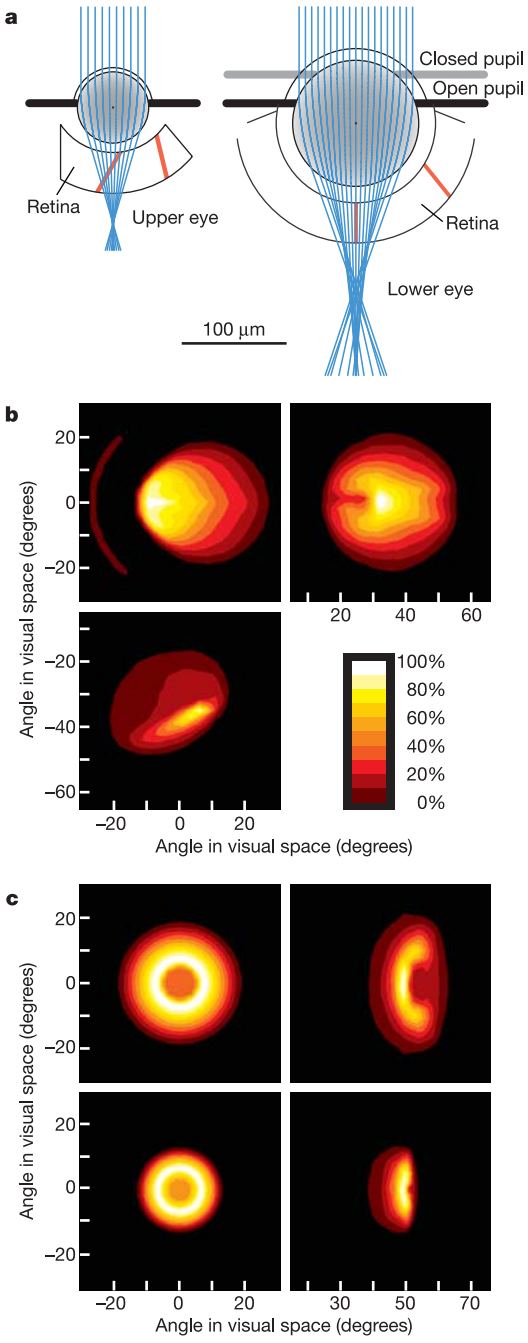

Figure 3 Modelling of receptive fields of individual photoreceptors in the retina of the upper and lower eyes. **a**, The optical models were used for tracing rays through the lens and retina and computing the absorption of light in selected single photoreceptors (red bars). Rays were traced in three dimensions, and by calculating receptor absorption at different incident angles of the ray bundle it was possible to generate receptive field maps for any receptor in the eyes. **b**, **c**, Receptive fields of receptors in the upper eye (**b**) and the lower eye (**c**). The top panels in **b** are for the central and peripheral receptors in the upper eye, as indicated in **a**. Note that the tilted receptors cause asymmetric receptive fields. The bottom panel in **b** shows the receptive field of a peripheral receptor in the perpendicular plane of the upper eye (see frontal view in Fig. 1d). Because the lower eye (**c**) is rotationally symmetrical, the perpendicular plane is identical with that shown in **a**. The top panels are modelled with an open pupil, for central (left) and peripheral (right) receptors (see red bars in **a**). The bottom panels are for the same receptors under a closed pupil. The sensitivity of the receptors was normalized to 100% in accordance with the colour map in **b**.

To analyse the consequence of under-focused optics and lack of light-guiding structures in the retina further, it is necessary to measure the angular sensitivity functions of individual photoreceptors. Normally, intracellular electrophysiological recordings would be the method of choice here, but we have not yet succeeded with this approach. However, our optical and anatomical data allow an alternative approach: calculations of light absorption in single receptors using a three-dimensional ray-path model. This approach has the advantage of allowing a direct correlation between the angular acceptance function of a receptor and its position in the retina. We traced three-dimensional beams of light in a fine angular matrix covering the visual field of the eye, and calculated the amount of light absorbed in selected photoreceptor cells as a function of the angle in visual space. The resulting maps are the complete angular sensitivity functions (receptive fields) of selected receptors (Fig. 3).

As expected from the severe under-focusing, the receptive fields are very wide compared with those of photoreceptors in other eyes. Half-widths of the receptive fields are about 20°, which is to be compared with a few degrees in insect compound-eye photoreceptors, and much less than 1° in vertebrate camera-eye photoreceptors[13]. If they had light-guiding photoreceptors in the focal plane of the lens, both the upper and lower eye of *Tripedalia* would easily be able to obtain angular sensitivities less than 1°. The visual resolution is thus very much worse than the sophisticated lenses would allow. Another peculiarity of the receptive fields is their shape. Central receptors in the lower eye display a ring of highest sensitivity surrounding a pronounced dip, and other receptors have strongly non-concentric sensitivity functions (Fig. 3). A recurring feature in our modelled receptive fields is that the sensitivity peak is flanked by a steep slope on one side and a much slower decrease on the other. This indicates that higher spatial frequencies at certain orientations remain in the otherwise very blurred image.

Because we do not yet know how the visual information from the lens eyes of box jellyfish is processed and used, we cannot tell what purpose the peculiar sensitivity functions might serve. But it is intriguing to note that many neurons in higher visual centres of the vertebrate brain also have large and geometrically complex receptive fields[19–21]. A typical feature of animal visual systems is that higher processing occurs in parallel pathways where each pathway handles a specific aspect of information such as large-field motion detection or feature recognition[22]. The large and complex receptive fields of neurons found in vertebrate higher visual centres represent highly filtered information needed for specific visual tasks. In box jellyfish we find these large complex receptive fields at the level of photoreceptors, indicating that the eyes might be specialized for a specific task only and that this allows complex filtering of information much earlier than in more general visual systems. The fact that box jellyfish have four different types of eye gives support to the idea that each eye type is highly specialized.

The early evolution of animal visual systems is likely to have started out with eyes that were involved only in single visual tasks. In this perspective it is interesting to note that high visual acuity is not necessarily desirable. The lens eyes of box jellyfish indicate that there might be visual tasks best served by a blurred image. Evolution of sophisticated eyes might therefore be a process with discrete stages representing the sequential addition of visual tasks. Our results also indicate that advanced lenses with graded-index optics might have evolved for tailoring complex receptive fields and not just for improving sensitivity or acuity. □

Methods

Animals

Adult *Tripedalia cystophora* were collected in mangrove swamps near La Parguera, Puerto Rico. Experiments were performed on animals caught in the wild and on descendants cultured in the laboratory. We used medusae with a bell height of 6–8 mm.

Anatomical model

To obtain an anatomically precise model of the eye geometry we used sections of rhopalia prepared in fixative (2.5% paraformaldehyde, 2.5% glutaraldehyde and 3% sucrose in 0.1 M cacodylate buffer pH 7.4) for 2 h, dehydrated in an ethanol series and embedded in Epon resin. The plastic blocks were cut at 0.5 μm on a diamond knife and stained with methylene blue and azur blue. Sections for light microscopy were cut through the sagittal plane of the rhopalium and perpendicular to this plane along the optical axis of the upper and lower lens eyes respectively. Geometrical models were generated as an average based on eight rhopalia from different animals. The sections suffered some shrinkage and minor deformations, which was corrected in the model by comparison with photographs of 12 fresh rhopalia in which the outer margins of the lens and retina were visible. Photoreceptor dimensions were measured on material prepared as above but block-stained with OsO_4, sectioned for electron microscopy, post-stained with lead citrate and uranyl acetate, and examined in a Jeol transmission electron microscope.

Microinterferometry

Fresh lenses were dissected out of rhopalia with thin tungsten needles. The success rate was low, and only about one in every five trials resulted in an intact isolated lens. Dissections and subsequent measurements were made in marine salt water. The isolated lenses were placed in a parallel-sided cavity of strain-free glass, wide enough not to squeeze the lens. The cavity was placed in a Zeiss interference microscope (Jamin-Lebedeff type) fitted with interference condenser and objective for × 10 magnification. The measurement beam passed through the jellyfish lens, and the reference beam passed immediately next to it. Monochromatic light of wavelength 546 nm was used. The microscope was focusing at the widest part of the jellyfish lens, and the background phase shift was adjusted to maximum extinction. This double-beam interferometric setup produced concentric interference fringes in the lenses. From the position of the fringes, phase shift profiles were generated in 5 to 12 different directions from the centre to the periphery of each lens. Average phase shift profiles for each lens were then converted to refractive index profiles. The conversion, which assumes rotational symmetry, was performed with an iterative ray-tracing procedure[23]. Refractive index profiles were calculated for lenses of six upper and six lower eyes, and average profiles were fitted by cubic-spline functions.

Optical modelling

To generate receptive fields (Fig. 3), a matrix of 100,000 parallel rays, evenly spaced over 120 μm × 120 μm, were traced through the full pupil apertures of the upper and lower lens eye, using the measured refractive index gradients (Fig. 2) and the geometrical eye models (Figs 1d, 3a). The trajectory of each ray was calculated in steps of 0.05 μm, accounting for refraction at interfaces and in the lens gradient (see ref. 23 for equations). The water surrounding the eye was given a refractive index of $n = 1.33$, the cellular lens capsule $n = 1.34$ and the retinal receptors $n = 1.36$. The retina was assumed to absorb light with an absorption coefficient of 0.01 μm^{-1}, which is a typical value for receptive segments of photoreceptors with microvilli[24]. Receptors were modelled as cylindrical structures, and absorption in a selected target receptor provided the calculated output from each ray tracing. The incident angle of the ray matrix was changed in increments of 1° in one plane, and the other plane was accessed by rotating the arc of different incident angles azimuthally in steps of 5°. Data on the receptive field are thus most densely sampled in the centre of the visual field. The ray-tracing program was written in Pascal (Metrowerks CodeWarrior), and the response data were plotted by using Mathworks MATLAB with cubic-spline interpolation.

Received 29 November 2004; accepted 21 February 2005; doi:10.1038/nature03484.

1. Buskey, E. J. Behavioral adaptations of the cubozoan medusa *Tripedalia cystophora* for feeding on copepods (*Dioithona oculata*) swarms. *Mar. Biol.* **142,** 225–232 (2003).
2. Berger, E. W. The histological structure of the eyes of cubomedusae. *J. Comp. Neurol.* **8,** 223–230 (1898).
3. Laska, G. & Hündgen, M. Morphologie und Ultrastuktur der Lichtsinnesorgane von *Tripedalia cystophora* Conant (Cnidaria, Cubozoa). *Zool. Jb. Anat.* **108,** 107–123 (1982).
4. Coates, M. M. Visual ecology and functional morphology of the Cubozoa. *Integr. Comp. Biol.* **43,** 542–548 (2003).
5. Nilsson, D.-E. Eye evolution: a question of genetic promiscuity. *Curr. Opin. Neurobiol.* **14,** 407–414 (2004).
6. Arendt, D., Tessmar-Raible, K., Snyman, H., Dorrestein, A. W. & Wittbrodt, J. Ciliary photoreceptors with a vertebrate-type opsin in an invertebrate brain. *Science* **306,** 869–871 (2004).
7. Stewart, S. E. Field behavior of *Tripedalia cystophora* (Class Cubozoa). *Mar. Freshwater Behav. Physiol.* **27,** 175–188 (1996).
8. Martin, V. J. Photoreceptors of cnidarians. *Can. J. Zool.* **80,** 1703–1722 (2002).
9. Piatigorsky, J. & Kozmik, Z. Cubozoan jellyfish: an evo/devo model for eyes and other sensory systems. *Int. J. Dev. Biol.* **48,** 719–729 (2004).
10. Laska, G. & Hündgen, M. Die Ultrastruktur des neuromuskulären Systems der Medusen von *Tripedalia cystophora* und *Carybdea marsupialis* (Coelenterata, Cubozoa). *Zoomorphology* **104,** 163–170 (1984).
11. Piatigorsky, J., Horwitz, J. & Norman, B. L. J1-crystallins of the cubomedusan jellyfish lens constitute a novel family encoded in at least three intronless genes. *J. Biol. Chem.* **268,** 11894–11901 (1993).
12. Piatigorsky, J. *et al.* J3-crystalline of the jellyfish lens: Similarity to saposins. *Proc. Natl Acad. Sci. USA* **98,** 12362–12367 (2001).
13. Land, M. F. & Nilsson, D.-E. *Animal Eyes* (Oxford Univ. Press, Oxford, 2002).
14. Kröger, R. H. H., Campbell, C. W., Munger, R. & Fernald, R. D. Refractive index distribution and spherical aberration in the crystalline lens of the African cichlid fish *Haplochromis burtoni*. *Vision Res.* **34,** 1815–1822 (1994).
15. Werner, B., Cutress, C. E. & Studebaker, J. P. Life cycle of *Tripedalia cystophora* Conant (Cubomedusae). *Nature* **232,** 582–583 (1971).
16. Jagger, W. S. & Sands, P. J. A wide-angle gradient index optical model of the crystalline lens and eye of the octopus. *Vision Res.* **39,** 2841–2852 (1999).

17. Fletcher, A., Murphy, T. & Young, A. Solutions of two optical problems. *Proc. R. Soc. Lond. A* **223,** 216–225 (1954).
18. Stange, G. The ocellar component of flight equilibrium control in dragonflies. *J. Comp. Physiol. A* **141,** 335–347 (1981).
19. DeAngelis, G. C., Ghose, G. M., Ohzawa, I. & Freeman, R. D. Functional micro-organization of primary visual cortex: receptive field analysis of nearby neurons. *J. Neurosci.* **19,** 4046–4064 (1999).
20. Suder, K. *et al.* Spatial dynamics of receptive fields in cat primary visual cortex related to the temporal structure of thalmocortical feedforward activity. *Exp. Brain Res.* **144,** 430–444 (2002).
21. Schweigart, G. & Eysel, U. T. Activity dependent receptive field changes in the surround of adult cat visual cortex lesions. *Eur. J. Neurosci.* **15,** 1585–1596 (2002).
22. Bartels, A. & Zeki, S. The theory of multistage integration in the visual brain. *Proc. R. Soc. Lond. B* **265,** 2327–2332 (1998).
23. Nilsson, D.-E., Andersson, M., Hallberg, E. & McIntyre, P. A micro-interferometric method for analysis of rotation-symmetric refractive-index gradients in intact objects. *J. Microsc.* **132,** 21–29 (1983).
24. Warrant, E. J. & Nilsson, D.-E. Absorption of white light in photoreceptors. *Vision Res.* **38,** 195–207 (1998).

Acknowledgements We thank E. J. Warrant and M. F. Land for comments on the manuscript, and Rita Wallén for technical assistance. This work was supported by grants from the Swedish Research Council (to D.-E.N.), the National Science Foundation USA (to M.M.C.) and the Danish Research Council (to A.G.).

Competing interests statement The authors declare that they have no competing financial interests.

Correspondence and requests for materials should be addressed to D.-E.N. (dan-e.nilsson@cob.lu.se).

The flight paths of honeybees recruited by the waggle dance

J. R. Riley[1], U. Greggers[2], A. D. Smith[1], D. R. Reynolds[3] & R. Menzel[2]

[1]*Plant and Invertebrate Ecology Division, Rothamsted Research, Harpenden, Hertfordshire AL5 2JQ, UK*
[2]*Freie Universität Berlin, Fachbereich Biologie, Chemie, Pharmazie, Institut für Biologie - Neurobiologie, 28–30 Königin-Luise-Strasse, D-14195, Berlin, Germany*
[3]*Plant, Animal and Human Health Group, Natural Resources Institute, University of Greenwich, Central Avenue, Chatham, Kent ME4 4TB, UK*

In the 'dance language' of honeybees[1,2], the dancer generates a specific, coded message that describes the direction and distance from the hive of a new food source, and this message is displaced in both space and time from the dancer's discovery of that source. Karl von Frisch concluded that bees 'recruited' by this dance used the information encoded in it to guide them directly to the remote food source, and this Nobel Prize-winning discovery revealed the most sophisticated example of non-primate communication that we know of[3,4]. In spite of some initial scepticism[5–9], almost all biologists are now convinced that von Frisch was correct[3,4,10–14], but what has hitherto been lacking is a quantitative description of how effectively recruits translate the code in the dance into flight to their destinations. Using harmonic radar[15–17] to record the actual flight paths of recruited bees, we now provide that description.

There have been some important advances since von Frisch's original experiments, and it has been believed for some time that the honeybee communication system does not instantly specify a food location to the recruits, without any hesitancy and with pinpoint accuracy[18]. In fact, detailed observations have shown that recruits may go through several iterations of dance session and resultant search flight before they eventually arrive at the indicated food source, and some never find the food at all[3,19–21]. The current interpretation of the von Frisch hypothesis thus predicts that newly recruited bees should fly directly from the hive to the vicinity of a food source, and then proceed to search for its exact location using odour and other cues[2]. This searching period would neatly account for the fact that the arrival of recruits at the source is often very much later than would be expected for a direct flight between the hive and food source—the anomaly that caused the initial scepticism about the hypothesis.

We began our experiments by capturing recruited bees as they left our observation hive, attaching a harmonic transponder, and then releasing them. The hive was not equipped to make quantitative measurements of individual dance angles or frequencies, but we observed that, at any given time, the dances of bees that had been previously recorded at the feeder were almost all aligned about a common direction. At midday this direction was at about 90° to the vertical, and this confirmed our expectation that the bees were feeding exclusively at our artificial feeder that lay 200 m directly east of the hive, and that it was to this food source that the waggle dances referred. Neither the feed nor the feeder station itself carried any artificial scents at any time.

Most recruited bees released from the hive almost immediately undertook a straight flight of direction and length that brought them directly into the vicinity of the feeder, as shown by the 19 flight paths from the hive in the upper part of Fig. 1. Figure 2a demonstrates that the mean direction of these flights lay impressively close to the hive-to-feeder direction for the first 200 m or so but, in spite of this, only two of the recruits actually found and alighted on the feeder. This was not a surprising result, given that similar low rates of success in finding unscented feeders have been found in conventional studies of recruit flight[22]. At the end of their straight outward flights, some recruits promptly initiated fairly direct return flights to the hive, but more usually they engaged in what appeared to be local searching manoeuvres for several minutes. It was noticeable that searching bees occasionally passed within just a few metres of the feeder without finding it, and in a few cases, searches lasted as long as 20 min, taking recruits as far as 200 m from the feeder location. These bees often returned to the point at which they had begun their searching behaviour before flying back to the hive, but fairly direct homeward flights from other points were also seen.

In a parallel experiment, recruited bees captured leaving the hive were taken to three release points 200–250 m away, and then

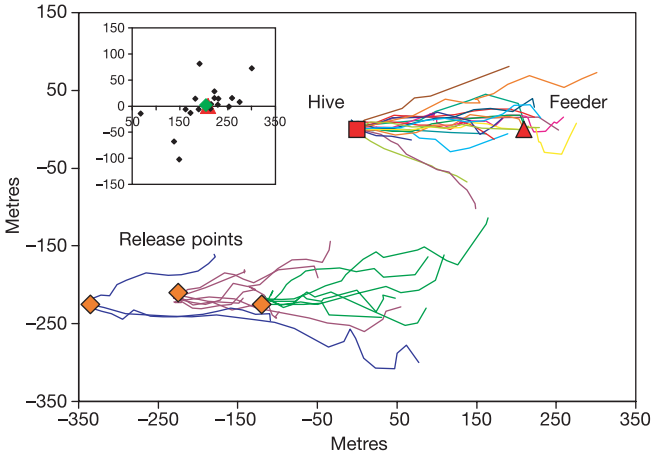

Figure 1 Flight paths of bees leaving the hive or other release points, after they had followed a waggle dance. Initial flight paths of 19 recruits leaving the hive (individual tracks in different colours) and of 17 recruits taken to locations southwest of the hive (different colour for each release point) before being released. The majority flew very close to the hive-to-feeder direction (90°), irrespective of where they were released. The tracks were truncated where they deviated by more than 90° from the hive-to-feeder direction over a track distance of more than 8 m, and this gave a mean length of 206 ± 53 m (s.d.) for hive-released bees, and 188 ± 94 m for the displaced bees. The corresponding straightness ratios (start–end point separation/track length) were 0.89 ± 0.07 and 0.82 ± 0.08. The end-point scatter of the hive-released recruits (inset) illustrates the imprecision of the dance communication/flight navigation system, but the close proximity of the mean end point (green diamond) to the feeder (red triangle) shows that, on average, the system is remarkably accurate.